Sustainable Energy & Fuels

High Capacity Vanadium Oxide Electrodes: Effective Recycling through Thermal Treatment

Journal:	*Sustainable Energy & Fuels*
Manuscript ID	SE-ART-03-2019-000188.R2
Article Type:	Paper
Date Submitted by the Author:	01-Jun-2019
Complete List of Authors:	Huang, Jianping; Stony Brook University Housel, Lisa; Stony Brook University Wang, Lei; Brookhaven National Laboratory Bruck, Andrea; Stony Brook University, ; Quilty, Calvin; Stony Brook University Abraham, Alyson; Stony Brook University Lutz, Diana; Stony Brook University, Chemistry Tang, Christopher; Stony Brook University, Kiss, Andrew; Brookhaven National Laboratory Thieme, Juergen; Brookhaven National Laboratory, National Synchrotron Light Source II Takeuchi, Kenneth; Stony Brook University Takeuchi, Esther; Stony Brook University Marschilok, Amy; Stony Brook University

High Capacity Vanadium Oxide Electrodes:

Effective Recycling through Thermal Treatment

Jianping Huang[a‡], Lisa M. Housel[a‡], Lei Wang[b], Andrea M. Bruck[a], Calvin D. Quilty[a], Alyson Abraham[a], Diana M. Lutz[a], Christopher R. Tang[c], Andrew Kiss[d], Juergen Thieme[d], Kenneth J. Takeuchi[a,c*], Esther S. Takeuchi[a,b,c,*], Amy C. Marschilok[a,b,c*]

a. Department of Chemistry, Stony Brook University, Stony Brook, NY 11794
b. Energy Sciences Directorate, Brookhaven National Laboratory, Upton, NY 11973
c. Department of Materials Science and Chemical Engineering, Stony Brook University, Stony Brook, NY 11794
d. National Synchrotron Light Source II, Brookhaven National Laboratory, Building 743, Upton, NY 11973-5000

‡ authors contributed equally to the manuscript

*corresponding authors: (KJT) kenneth.takeuchi.1@stonybrook.edu, (EST) esther.takeuchi@stonybrook.edu, (ACM) amy.marschilok@stonybrook.edu

Keywords

vanadium oxide, recycling, regeneration, lithium ion battery, capacity retention, x-ray diffraction, x-ray absorption spectroscopy

Broader Context

Integration of electrochemical energy storage devices into the electricity grid and electric vehicles is driven in part by a global effort towards energy and environmental sustainability. With sustainability as the target, it is critical that batteries have long lifetimes and this is being pursued by investigation and resolution of degradation modes. However, another approach is the recycling or regeneration of battery components enabling battery systems to have extended lifetimes. Further, effective recycling of battery components can expand the elemental compositions of materials that can be considered as practical enabling broader design options to meet the needed functional parameters. This study considers a high capacity vanadium oxide, V_2O_5, that after extended electrochemical (dis)charge cycling forms low capacity ω-$Li_xV_2O_5$. Recycling of the electrochemically cycled material results in formation of a new high capacity crystalline phase, LiV_3O_8, transforming the poorly performing phase to one that yields even higher capacity than the original structure. This demonstration illustrates that phase conversion during a recycling process can be beneficial both in extending the lifetime of a battery and increasing the functional capacity.

Abstract

This study demonstrates that thermal regeneration is an effective approach to convert degraded phases to functioning electroactive materials, restore functional delivered capacity and recover material crystallinity while retaining the integrity of the parent electrode. V_2O_5 nanowires were synthesized through a facile hydrothermal method and used to fabricate V_2O_5/carbon nanotube

(CNT) binder free electrodes. Discharge of the V_2O_5-CNT electrodes coupled with *operando* energy dispersive x-ray diffraction shows no evidence of phase segregation throughout the 150 μm thick binder free electrodes indicating full utilization of a thick electrode. When V_2O_5 is highly electrochemically lithiated ($x > 2$ in $Li_xV_2O_5$), irreversible phase transformation to ω-$Li_xV_2O_5$ was observed, accompanied by a capacity decrease of ~40% over 100 cycles. A simple thermal treatment of the entire electrode results in a delivered capacity equal to or higher than the original value. Both phase conversion and an increase in material crystallinity as a result of thermal treatment are observed where structural analysis indicates the formation of $Li_1V_3O_8$. The electrode design approach with thick electrodes and functional thermal regeneration may provide a broader choice of electroactive materials through decreasing the environmental burden by extending the lifetime of energy storage systems.

Introduction

Integration of electrochemical energy storage devices into the electricity grid and electric vehicles is driven in part by a global effort towards energy and environmental sustainability.[1] With sustainability as the target, it is critical that batteries have long lifetimes and this is being pursued by investigation and resolution of failure modes such as structural degradation of the electrodes, transition metal dissolution, and dendrite formation.[2-4] Energy stored on invested (ESOI) analysis showed that an increase in energy storage cycle life by 10 fold would greatly relax energetic constraints for grid-scale storage and improve cost competitiveness of electrochemical energy storage technologies.[5] Thus, another approach worthy of exploration is the recycling or regeneration of the battery components enabling battery systems to have extended lifetimes.[6, 7] Additionally, effective recycling of battery components expands the elemental compositions of materials that can be considered as practical. Research on recycling battery anode materials is scarce, since recycling lithium from Li-based batteries in a cost-effective manner remains an unsolved technology challenge.[8] Hard carbon anode materials recycled from organic waste have been previously utilized in a sodium-ion battery system.[9] Battery recycling of cathode materials has been studied more extensively, such as C-S cathodes from recycling waste rubber[10], $LiCoO_2$ and $LiNi_{1/3}Co_{1/3}Mn_{1/3}O_2$ recycled from hydrothermal treatment followed by short annealing process[11]. Overall, battery recycling is highly desirable if recovery of cathodes can be achieved at a lower emissions and energy intensity than producing pristine cathode materials. In addition, battery recycling is beneficial for reducing solid waste productions and addressing material scarcity concerns.[8, 12]

Conventional recycling processes are multistep, including mechanical, thermal and chemical separation stages.[7, 13-15] In these sequences, chemical leaching with highly corrosive acids or bases in addition to chemical precipitation or electrolysis is required to digest the electrode and completely recover transition metal components.[13, 16-18] Recent procedures have adopted more benign chemical agents such as D,L-malic acid or L-tartaric acid to leach metal ions from spent $LiNi_{1/3}Co_{1/3}Mn_{1/3}O_2$.[19, 20] Thermal treatment has also proved effective to reuse $LiFePO_4$ electroactive material, where the regenerated material exhibited comparable electrochemical properties to fresh $LiFePO_4$.[21] Similar heat treatments were adopted for $LiNi_{1/3}Co_{1/3}Mn_{1/}3O_2$ and $LiCoO_2$ regeneration.[22-25] However, the use of thermal treatment in these studies entailed smashing, soaking, heating, washing or centrifuging steps, which were required to separate the electroactive material from other components of the electrode (i.e. carbon, binder, current collector). A simpler, more direct washing/heating approach was applied to commercial lithium

based MnO_2 cells. However, the regenerated electroactive material was repurposed as a catalyst rather than a battery electrode.[26] A recycling strategy for a cathode based on tunnel structured manganese dioxide (α-MnO_2 structured K_xMnO_2) fibers has been reported.[6] Each time the recycling process was performed, average manganese oxidation state, crystallinity, and delivered capacity of ~110 mAh/g for the tunneled K_xMnO_2 were restored.

A layered structure capable of multiple electron transfers per metal center, V_2O_5 can theoretically provide a capacity of >440 mAh/g with three molar equivalents of lithiation, higher than the extensively studied NMC type materials such as $LiNi_{1-x-y}Mn_xCo_yO_2$ and Li-rich oxides ($Li_{1+x}M_{1-x}O_2$, M = Co, Mn, and Ni) still largely limited to <200 mAh/g.[27-30] Prior literature has demonstrated insertion of lithium ions into the V_2O_5 structure with a capacity ~280 mAh/g above 2.0 V.[31] Further, nanostructured V_2O_5 materials have been reported to improve the electrochemical performance of V_2O_5, such as hollow microflowers,[32] porous microspheres,[33] and leaf-like nanosheets.[34] For example, the capacity of V_2O_5 hollow microflowers remained above 200 mAh/g after 100 cycles,[32] and a V_2O_5 electrodeposited electrode exhibited a maximum specific capacity of 137 mAh/g with stable cycle performance delivering at ~40 mAh/g when cycled at 2 - 4 V over 1600 cycles at a 4C rate.[35] However, complicated phase transitions (α-ε-δ-γ-ω) may occur under electrochemical lithiation, and irreversible phase change to γ-$Li_2V_2O_5$ and ω-$Li_3V_2O_5$ has been observed to lead to capacity fade.[31, 36] As V_2O_5 is a promising high energy cathode material for lithium based batteries, appropriate recycling of vanadium-based electrodes is crucial to its widespread implementation to avoid concerns regarding the impact of vanadium on the environment.

In this work, V_2O_5 nanofibers were synthesized via a facile hydrothermal method and incorporated into a carbon nanotube matrix to produce binder-free electrodes. These V_2O_5/CNT electrodes were used for electrochemical testing, recovered, thermally treated, and reused in electrochemical cells. Thermal treatment of cycled V_2O_5/CNT electrodes is demonstrated herein for the first time, including demonstration of a capacity for the regenerated electrodes exceeding 200 mAh/g. The thermal regeneration mechanism was investigated by probing the pristine and regenerated electrodes via *ex-situ* x-ray diffraction, *ex-situ* x-ray absorption spectroscopy, and *operando* energy dispersive x-ray diffraction. Both phase conversion and an increase in material crystallinity as a result of thermal treatment are observed where structural analysis indicates the formation of $Li_1V_3O_8$. The electrode design approach with thick electrodes and functional thermal regeneration may provide a broader choice of electroactive materials through decreasing the environmental burden by extending the lifetime of energy storage systems. This demonstration illustrates that phase conversion during a recycling process can be beneficial both in extending the lifetime of a battery and increasing the functional capacity.

Results and Discussion

Electrode Design and Preparation

The V_2O_5 nanowires synthesized via the hydrothermal process were characterized by XRD, and all the peaks can be assigned to orthorhombic V_2O_5 (JCPDS # 89-0611) with lattice parameters of a = 11.544 Å, b = 4.383 Å, and c = 3.571 Å, **Figure 1a**. The layered structure is formed by the stacking of square pyramidal VO_5 units along axis b and is displayed as the inset in **Figure 1a**. A composite electrode design utilizing the fibrous active material combined with carbon nanotubes (CNT) was developed to eliminate the need for polymeric binders in the structure. The V_2O_5/CNT composite electrodes were prepared via a facile method where a suspension of

dispersed V_2O_5 nanowires and carbon nanotubes was filtered to prepare the paper-like V_2O_5/CNT composite electrodes, **Figure 1b**. Four types of binder free electrodes were prepared using different V_2O_5/CNT ratios ranging in color from yellow for the pure V_2O_5 electrode (V_2O_5/CNT-0) to black with high CNT content, **Figure 1c**. The CNT content was verified by thermogravimetric analysis (TGA) (**Figure S1**). The weight loss occurring at ~400°C is attributed to the oxidation of CNT consistent with previous reports on V_2O_5/CNT composites.[37, 38] Based on the TGA results, the CNT contents for the composites are 0, 12, 24 and 37% by mass for V_2O_5/CNT-0, V_2O_5/CNT-1, V_2O_5/CNT-2 and V_2O_5/CNT-3, respectively. The binder free electrodes have thicknesses of 0.15 ± 0.01 mm. The resistance of the electrodes was measured using a 4-point probe resistivity method and the electrode resistivity drops by 6 orders of magnitude with the incorporation of CNT (**Figure S2**). The resistivity values measured were 2.6 × 10^5, 0.23, 0.11 and 0.04 Ω·cm for V_2O_5/CNT-0, V_2O_5/CNT-1, V_2O_5/CNT-2 and V_2O_5/CNT-3, respectively.

The morphology and ordering of a V_2O_5/CNT-3 binder-free electrode were determined by scanning electron microscopy (SEM), **Figure 1d-g**. The as-prepared V_2O_5 materials were long fibers measuring 20-50 μm in length and ~50 nm in diameter appearing uniformly dispersed within the intertwined CNT network, both in the top-view image (**Figure 1d, e**) and in the side-view image (**Figure 1f, g**). The freestanding and flexible electrode has an average thickness of 0.15 mm (**Figure 1f**). To further investigate the distribution of the V_2O_5 fibers within the electrode, EDS elemental maps were acquired (**Figure S3)**, affirming effective dispersion of the synthesized V_2O_5 in the CNT network. Comparative SEM images (**Figure 2**, **Figure S4**) and EDS maps (**Figure S5**) were also acquired for the other V_2O_5/CNT electrode compositions, and collectively suggested dispersion of the V_2O_5 in the CNT network was best in the V_2O_5/CNT-3 electrode. XRD patterns of the V_2O_5/CNT-0, V_2O_5/CNT-1, V_2O_5/CNT-2, and V_2O_5/CNT-3 binder-free electrodes showed consistent patterns for the V_2O_5 material, with clearest evidence of the (002) peak attributable to CNT[39] in the V_2O_5/CNT-3 electrode with highest CNT content (**Figure S6**).

Electrochemistry of Binder Free Electrodes

Redox properties of the binder free electrodes were characterized by cyclic voltammetry (CV) measurements over a potential range of 4.0 to 2.0V where the results of cycle 2 of each composite electrode type are shown, **Figure 3a**. The multiple reduction and oxidation peaks in the V_2O_5/CNT electrodes are associated with the phase transitions of V_2O_5 under lithiation.[31, 34] V_2O_5/CNT-0 shows two cathodic peaks at 3.3 and 3.1 V, and one broad anodic peak at 3.7 V. In contrast, the CNT containing electrodes show three cathodic peaks at approximately 3.3, 3.1 and 2.2 V, corresponding to the phase changes (α-ε-δ-γ) with 0.5, 1.0, and 2.0 mol Li^+ intercalated into the cathode material, respectively.[40, 41] Anodic peaks for the CNT containing electrodes are located at approximately 2.52, 2.58, 3.26, 3.37 and 3.51 V, which indicate the phases undergo transformation from γ-$Li_2V_2O_5$ to the original phase α-V_2O_5. The additional peaks at 2.58 V and 3.51 V have been previously attributed to the phase transition of the γ- γ' system.[40, 42] The enhanced electrical conductivity due to the CNT incorporation results in higher peak currents and more clearly resolved voltammetric peaks with increasing CNT content.

Rate capability of the V_2O_5/CNT electrodes was investigated at currents ranging from 50 to 1000 mA/g of active material, **Figure 3b**. At 50 mA/g, the capacities of V_2O_5/CNT-1 (263 mAh/g), V_2O_5/CNT-2 (347 mAh/g) and V_2O_5/CNT-3 (330 mAh/g) are 2 -3 times higher than those of V_2O_5/CNT-0, indicating the benefit of the electrically conductive V_2O_5/CNT composite

electrode design. When the current density increases to 200 mA/g, the capacities of V_2O_5/CNT-0, V_2O_5/CNT-1, V_2O_5/CNT-2 and V_2O_5/CNT-3 are 56, 78, 226 and 216 mAh/g at cycle 10, respectively. V_2O_5/CNT-1 shows ~185 mAh/g capacity decrease (~70%) on increasing the current from 50 and 200 mA/g while V_2O_5/CNT-2 and V_2O_5/CNT-3 only show a ~120 mAh/g decrease (~20%). Interestingly, the electrochemistry of the electrode with12% CNT by mass in V_2O_5/CNT-1 is further improved by the inclusion of higher levels of CNT. V_2O_5/CNT-0 and V_2O_5/CNT-1 deliver low capacities at 500 mA/g (<30 mAh/g) while V_2O_5/CNT-2 and V_2O_5/CNT-3 deliver capacities of ~100 mAh/g and ~120 mAh/g, respectively. The improved capacity retention for the V_2O_5/CNT-3 with increasing current is illustrated in **Figure 3c**. The V_2O_5/CNT-3 sample shows the highest capacity at the highest current tested of 1000 mA/g highlighting the important role of electrical conductivity in the V_2O_5/CNT composite electrodes.

Under an applied current of the 50 mA/g, the V_2O_5/CNT-3 sample delivers a high initial capacity of 330 mAh/g corresponding to ~2.25 electron equivalents (e.e.) of Li ion insertion (**Figure 3d**). Four voltage plateaus at ~3.3, ~3.2, ~2.3 and ~2.0 V are observed, which correspond to the phase transitions from α-$Li_xV_2O_5$ to ε-, δ-, γ- and ω- $Li_xV_2O_5$, respectively.[31, 34, 36] Specifically, the phase transition of α-ε-δ occurs when x in $Li_xV_2O_5$ is ≤ 1.0 (<147mAh/g). Lithiations from 1.0 < x ≤ 2.0 and to x > 2.0 (294 mAh/g) are attributed to the δ-γ transition and γ-ω transitions, respectively.[31, 36] Notably, there is no clear voltage plateau upon charging, which was also observed in previous literature after Li insertion at values x > 2.0 (> 294 mAh/g).[31, 43] At higher current densities (200 and 500 mA/g), the both the discharge-charge voltage curves maintain slopping profiles without the appearance of clear voltage plateaus. The sloping shape of the voltage curve implies a solid solution process, which may result from the formation of ω-$Li_xV_2O_5$.[31, 44]

In order to verify the ω phase-induced solid solution mechanism, the V_2O_5/CNT-3 electrode was cycled under repetitive Coulombically controlled reduction with discharge by 2.25 molar electron equivalents (330 mAh/g) and a secondary voltage limit of 1.5 V, and charge to 4.0 V. The discharge voltage profile shows clear voltage plateaus at cycle 1 yet transforms to a smoother curve in the subsequent cycles, **Figure 4a**. By cycle 5, both discharge and charge curves no longer display the characteristic plateaus rather showing a sloping voltage profile reaching the terminal voltage of 1.5 V. With continued cycling, from cycles 5 to 30, the terminal voltage under discharge consistently reaches the voltage limit (1.5 V). As a result, the lithiation level decreased from 2.25 to 1.50 electron equivalents (**Figure 4b**). The recovered electrode was further examined and the XRD pattern shows three distinctive peaks of ω-$Li_xV_2O_5$ at 38.8°, 44.5°, and 64.5°, respectively, consistent with prior XRD results reported on ω-$Li_xV_2O_5$.[31, 44] These peaks are indexed to the cubic structure of $Li_xV_{1-x}O$ (JCPDS # 089-3078) with lattice parameter a of 4.1 Å. Thus, the ω phase formed at x > 2.0 can lead to an irreversible phase change which occurs concomitantly with the degradation of the terminal voltage and capacity in Coulombically controlled cycling to high depth of discharge.

Operando Structural Characterization of Electrochemistry

The V_2O_5/CNT-3 electrode was investigated further using x-ray microfluorescence (μ-XRF) mapping and *operando* x-ray absorption near edge fine structure (XANES). The μ-XRF map of undischarged V_2O_5/CNT-3 suggests the V_2O_5 is well dispersed in the CNT matrix (**Figure 5a**). Prior to lithiation, the pre-edge peak position of the V_2O_5/CNT-3 electrode (5470.8 eV) is within error (0.5 eV) of the V_2O_5 powder standard (5470.5 eV), **Figure 5b**, suggesting an initial oxidation state of V^{5+}. The absolute pre-edge peak position of the XANES spectra shifts linearly

towards lower energy during the 50 mA/g discharge to $Li_{2.0}V_2O_5$, consistent with vanadium oxidation state reduction (**Figure 5c, d, e**).[45, 46] At $Li_{2.0}V_2O_5$, the pre-edge peak position matches the most intense peak in the pre-edge of the VO_2 standard (5469.3 eV), indicating electrochemical reduction to V^{4+} (**Figure 5b**).

Energy dispersive x-ray diffraction (EDXRD) data was collected during the first cycle of electrochemical (de)lithiation to determine the spatial and temporal evolution of a V_2O_5/CNT-3 electrode within an intact lithium based electrochemical cell. With use of a bright synchrotron light source enabling a small gauge volume, the EDXRD experiment provided tomographic monitoring of the phase changes to determine the possible phase segregation that have been previously observed to limit reversibility for other V_xO_y electrodes.[20] The EDXRD scans in **Figure 6** show electrodes where the scan initiated at the Li anode interface and continued to scan to the current collector of the cell. The region between 0.29 – 0.4 $Å^{-1}$ was monitored to evaluate the structural variation throughout the thickness of the electrode during electrochemical (dis)charge. The separation of the V_2O_5 (400) and (310) reflections (1/d = 0.3452 and 0.3496 $Å^{-1}$) in the 'undischarged' scan collected prior to onset of electrochemical reduction is consistent with some degree of lithiation before electrochemical testing, likely from self-discharge during two weeks prior to the EDXRD measurement. Additional evidence of self-discharge is provided by the lower delivered discharge capacity of ~275 mAh/g for this cell (where capacities >300 mAh/g were consistently observed when the cells had no rest before discharge). Therefore, the scan 1 EDXRD data are indexed as $Li_xV_2O_5$ (400) and $Li_xV_2O_5$ (310) in **Figure 6**. The initial lithium insertion from x = 0 – 0.7 in $Li_xV_2O_5$ is generally considered to move from the α- to ε-structure with very little structural variation between the two polymorphs and only a peak shift observed upon lithium intercalation and expansion of the parent structure.[47] From scan 1 to 2 the peaks separate from one another consistent with a transformation from the α- to the ε-$Li_xV_2O_5$ structure.[47] At scan 3, during the onset of the second plateau around 2.25 V the δ-$Li_xV_2O_5$ (111) and (112) peaks emerge, which agrees well with previous literature. At the final discharged state (with ~275 mAh/g reached) the γ- $Li_xV_2O_5$ (023) and (004) reflections at 1/d = 0.3402 and 0.3669 $Å^{-1}$ were the predominant phase observed with no ω- $Li_xV_2O_5$ detected (1/d = 0.3 – 0.6 $Å^{-1}$ shown in **Figure S7**). Upon charge, the reverse process occurs with homogenous phase transformations throughout the thickness of the electrode with major intensity at approximately 1/d = 0.347 $Å^{-1}$ consistent with the $Li_xV_2O_5$ (400) and (310) reflections. Notably, uniform phase transformations were observed throughout (dis)charge and charge, as shown in **Figure 6**. This high degree of homogeneity during discharge indicates the opportunity for full utilization of the active materials in this binder-free electrode construction.

Thermal Regeneration

Cells with the V_2O_5/CNT-3 configuration were put on long term cycling test in a voltage window of 4.0-2.0 V at 200 mA/g after completion of the 20 cycle rate capability test, **Figure 7a**. V_2O_5/CNT-3 delivers a capacity of 216 mAh/g at cycle 21 and the discharge and charge curves display a sloped profile, **Figure 7b**. Between cycle 21 to cycle 120, the capacity decreases steadily with ~0.9 mAh/g loss per cycle. A control V_2O_5/CNT-3 electrode was used to verify the impact of thermal treatment on capacity recovery (**Figure 7a**). The electrode was cycled at 200 mA/g, recovered after 100 cycles, and assembled in a new cell without thermal treatment. This cell containing the electrode without heat treatment shows only a small capacity recovery from 144 to 172 mAh/g, therefore the testing of this cell was stopped after 200 cycles. In contrast, the regenerated electrode shows a much more significant recovery from 123 to 263 mAh/g. The difference in the protocols between the regenerated electrode and control electrode is the

inclusion of the thermal treatment step that is demonstrably important for the significant capacity recovery. The electrochemistry of the thermally treated electrode is discussed in additional detail below.

To achieve thermal regeneration, the V_2O_5/CNT-3 electrode was recovered from a cell after cycle 120 and regenerated by a simple 300^{o}C two hour heat treatment. After the thermal regeneration, the electrode was used in a new cell and returned to test. Notably, the regenerated electrode cell delivers a high capacity of 230 mAh/g at cycle 121 (the first cycle after the regeneration). The capacity increases to 263 mAh/g at cycle 122, consistent with the charge capacity at cycle 121, **Figure 7c**. From cycle 121 to cycle 220, the regenerated electrode cell displays capacity fade with a capacity decreases of ~1.0 mAh/g per cycle. Due to the excellent response of the cell containing the regenerated electrode on the first regeneration, a second regeneration with additional cycling was undertaken. On second regeneration was conducted after cycle 220, and the capacity recovers from 159 mAh/g to 243 mAh/g after regeneration demonstrating that the heat treatment is effective at recovering the functional capacity, **Figure 7a.**

The capacity increases after the first and second regeneration step are observed to be 140 mAh/g and 84 mAh/g, respectively. However, the control electrode without the thermal regeneration step only shows a 28 mAh/g increase in delivered capacity.

Interestingly, the discharge and charge voltage profiles significantly change after the regeneration process. The discharge curves show multiple plateaus with a flat voltage plateau at 2.5 V, **Figure 7d**. This voltage profile does not resemble that of V_2O_5 nor ω-$Li_xV_2O_5$, implying formation of a new phase after the 1st regeneration, which was identified using XRD structure analysis as detailed in the text below. Notably, the discharge and charge voltage profiles after the second regeneration sequence (cycles 222-320), **Figure 7e** remain consistent to those observed after the first regeneration, **Figure 7d**.

To further validate the consistent voltage profile of the material after regeneration, the energy density was plotted as a function of cycle number, **Figure 7f**. The thermal regeneration is effective to maintain capacity >150 mAh/g and energy density >414 mWh/g for 100 cycles. After the 1st regeneration, the energy density reaches 727 mWh/g, which gradually decreases to 440 mWh/g after an additional 100 cycles (**Figure 7f**). An average energy density of 565 mWh/g is delivered over the 100 cycles. After the 2nd regeneration, the energy density is restored to 665 mWh/g, and an average energy density of 508 mWh/g is delivered from cycle 221 to cycle 320. Thus, the 2nd regeneration process effectively restores both caapcity and voltage (energy) of the material consistent with the 1st regeneration.

Structural Analysis of Regenerated Electrodes

XRD patterns were collected to analyze the structural changes for the V_2O_5/CNT-3 electrode before cycling, after cycle 120, and after the 1st regeneration, **Figure 8**. Before cycling, the XRD pattern shows intense peaks of the V_2O_5 phase with a broad peak at ~25° assigned to CNT. After cycle 120, the characteristic V_2O_5 diffraction peaks are absent, and the peak intensities show significant decreases. Two broad peaks at ~44° and ~64° are notable and are assigned to ω-$Li_xV_2O_5$. The other new peaks agree with the diffraction peaks of γ-$Li_xV_2O_5$ (JCPDS # 73-1340). Based on the XRD pattern of cycled electrode, V_2O_5 phase is irreversibly converted to ω-

and γ- $Li_xV_2O_5$ phases after the electrochemical cycling in 4.0-2.0 V. ω-$Li_xV_2O_5$ is a disordered rocksalt type structure where Li and V occupy the same octahedral sites. The rocksalt lattice forms when the material is lithiated to ω-$Li_3V_2O_5$ ($Li_{0.6}V_{0.4}O$), and the de-lithiated form of ω-$Li_xV_2O_5$ retains the same structure by possessing cationic vacancies.[31, 44] Thus, the irreversible phase change is consistent with the observed capacity fade between cycle 21 and 120 as well as the sloping voltage profiles. After the 1st regeneration, the diffraction peaks of ω-$Li_xV_2O_5$ disappear, and an intense peak at ~14° occurs. The majority of the new peaks can be assigned to $Li_1V_3O_8$ (JCPDS # 86-2421), indicating $Li_1V_3O_8$ is the major phase now present in the regenerated electrode. The other peaks present can be indexed to unreacted V_2O_5 and β-$Li_{2/3}V_2O_5$ (PDF card #01-074-0054), a layered phase that is structurally similar to $Li_1V_3O_8$. No peaks corresponding to the γ-, δ-, ε-, or ω-$Li_xV_2O_5$ phases were observed. The phase conversion from ω-$Li_xV_2O_5$ to $Li_1V_3O_8$ under heat treatment may be rationalized by the instability of rocksalt structure with cationic vacancies. Interestingly, the discharge and charge voltage profiles (**Figure 7c**) for the regenerated electrode are consistent with reported voltage profiles of $Li_1V_3O_8$,[20, 48] further indicating the formation of a new electrochemically active phase.

EDXRD data was collected during the first cycle of electrochemical (de)lithiation to determine the structural evolution of the regenerated V_2O_5/CNT-3 electrode. The EDXRD scans in **Figure 9** show the electrode where the scan initiated at the Li anode interface and scans continued to the current collector of the cell. The region between 0.27 – 0.4 $Å^{-1}$ was monitored to evaluate the structural variation throughout the thickness of the electrode during electrochemical (dis)charge. The EDXRD scans reveal that the (dis)charge occurs relatively homogeneously with no significant phase segregation observed. In the initial scan (**Figure 9, Scan 1**), four peaks are observed between 0.27 and 0.4 $Å^{-1}$ at 0.294, 0.322, 0.345, and 0.368 $Å^{-1}$. These peaks are assigned to β-$Li_{2/3}V_2O_5$ ($11\bar{1}$), β-$Li_{2/3}V_2O_5$ (003), $Li_1V_3O_8$ (103), and V_2O_5 (011) respectively. During discharge (**Figure 9, Scans 3 and 4**), the (103) and (011) peaks disappear suggesting the $Li_1V_3O_8$, and V_2O_5 phases amorphize during discharge. The ($11\bar{1}$) and (003) peaks shift from 0.294 and 0.322 $Å^{-1}$ to 0.289 and 0.307 $Å^{-1}$ consistent with a lattice expansion of the β-$Li_{2/3}V_2O_5$ during lithiation. A new peak is observed at 0.281 $Å^{-1}$, this peak can be assigned to the (011) peak of the γ-$Li_xV_2O_5$ phase. During the charge step (**Figure 9, Scans 6,8, and Full charge**), the V_2O_5 and $Li_1V_3O_8$ peaks reappear, the γ-$Li_xV_2O_5$ peak disappears, and the β-$Li_{2/3}V_2O_5$ peaks return to their original positions. This shows that the discharge of the regenerated V_2O_5/CNT pellet is reversible.

The cycled electrode after cycle 220 remains $Li_1V_3O_8$ phase with slightly decreased diffraction peaks intensities, **Figure 10a**. The peaks in the diffraction angle regions of ~14° and 40°-44° are compared **(Figure 10b** and **10c**). In addition to the decreased peak intensities, broadening of the peaks at ($50\bar{2}$) ~41° and (302) ~43° is observed in the cycled electrode, indicative of decreased crystallinity. A prior study on lithiation of $Li_1V_3O_8$ has shown that the lattice b increases by 11% and lattice c decreases by 8% when $Li_1V_3O_8$ is lithiated to $Li_4V_3O_8$ (279 mAh/g).[20] The large lattice changes in the two directions (b and c) may lead to disordered layer stacking and decreased crystallinity in c direction. After the 2nd regeneration, the (001) peak at ~14° becomes more intense, and the ($50\bar{2}$) and (302) peaks are restored.

The Scherrer equation was used to estimate crystallite sizes of the active material after the 1st regeneration, after electrochemical cycling, and after the 2nd regeneration, **Table 1**.[49] After 100 cycles from cycle 121 to cycle 220, the crystallite size based on (001) plane decreases from 39 nm to 27 nm due to the lattice c change under repeated cycling. The sizes based on ($50\bar{2}$) and

(302) planes show 8 nm and 14 nm decreases, respectively. After the 2nd regeneration, the crystallite sizes show 10-12 nm increases, indicating the recovery of material crystallinity. The regeneration based on crystallinity recovery was also reported in a previous study on α-MnO_2 type material, where the regeneration restored the capacity successfully.[6]

In order to probe the V oxidation state and coordination environment for V_2O_5, the V x-ray absorption (XAS) K-edge was measured for freshly regenerated $Li_1V_3O_8$ and cycled $Li_1V_3O_8$ - electrodes, **Figures 10d** and **10e**. The synthesized V_2O_5 electrode has an edge energy at 5480.5 eV consistent with reported values for V_2O_5.[50, 51] The regenerated and cycled $Li_1V_3O_8$ have similar XANES region with an edge energy value of 5482.8 eV. The pre edge peak at ~5470 eV results from the V 3d and 4p orbitals mixing. The 4p orbitals in square pyramidal VO_5 have the same symmetries (A1 and E) as some 3d orbitals, enabling the transition from 1s to 3d-4p. The Fourier transformed EXAFS spectra of regenerated $Li_1V_3O_8$ and cycled $Li_1V_3O_8$ are compared (**Figure 10e**). Two intense peaks at ~1.5 Å and ~2.6 Å are attributed to V-O and V-V scattering, respectively. The cycled $Li_1V_3O_8$ shows a similar peak intensity at ~1.5 Å as the regenerated $Li_1V_3O_8$. At radial distance >2.0 Å, the peaks intensities are lower in the cycled $Li_1V_3O_8$ than those in the regenerated $Li_1V_3O_8$, further demonstrating electrochemical cycling introduces structural disorder in $Li_1V_3O_8$ while regeneration recovers structural order consistent with the *ex-situ* XRD results.

Conclusion

V_2O_5 nanowires were synthesized and used to fabricate V_2O_5/CNT binder free electrodes. The inclusion of the CNT matrix increases the electrode electrical conductivity and the V_2O_5/CNT-3 with 37% CNT shows higher rate capability than electrodes with lower CNT content. When V_2O_5 is highly lithiated (x in $Li_xV_2O_5$ is >2), irreversible phase transformation to ω-$Li_xV_2O_5$ is observed, which leads to a capacity decrease from 216 to 123 mAh/g over 100 cycles. Thermal regeneration of the electrode restores the delivered capacity to 263 mAh/g capacity, even higher than the initial capacity for these electrodes.

Interestingly, structural analysis indicated that the thermal treatment of the cycled V_2O_5/CNT-3 electrodes converts the phase to $Li_1V_3O_8$. Repeated use of the thermal treatment continues to be effective for cycled $Li_1V_3O_8$ electrodes restoring crystallinity, vanadium coordination environment, and capacity.

This study demonstrates the thermal regeneration method is an effective method to convert unstable phases to functioning electrode materials, restore functional delivered capacity and recover material crystallinity. Furthermore, the full restoration of functional capacity after regeneration is achieved with no additional material processing or electrode processing required. This is notable as the active material represents a significant cost component of today's lithium ion battery, and both the time and cost involved in conventional electrode processing is significant.[52] The approach demonstrated here may enable a broader choice of electrode materials and provides an approach to decrease the environmental burden of energy storage systems.

Experimental Section

Materials synthesis and characterization V_2O_5 nanowires were synthesized using a hydrothermal method. V_2O_5 solid was added to distilled H_2O. Several drops of 30 % H_2O_2 were added with stirring. The orange solution was transferred to a hydrothermal bomb and heated at

205°C for 96 hours. After synthesis, the products were washed with distilled water and dried under vacuum. X-ray diffraction (XRD) was performed using a Rigaku SmartLab X-ray diffractometer with Cu Kα radiation and Bragg-Brentano focusing geometry.

Electrode preparation and characterization

As-synthesized V_2O_5 fibers and multiwall carbon nanotubes (CNT) were dispersed in1-methyl-2-pyrrolidone (NMP) with sonication. V_2O_5/CNT composites were prepared in mass/mass ratios of 1:0 (V_2O_5/CNT-0), 9:1 (V_2O_5/CNT-1), 4:1 (V_2O_5/CNT-2), and 1.5:1(V_2O_5/CNT-3). The suspensions were filtered and dried under vacuum. The paper-like V_2O_5/CNT composites were cut into 12.5 mm diameter, 150 µm thick binder free electrodes. Thermogravimetric analysis (TGA) was conducted using a TA instruments SDT Q600 under air flow. Electrode resistivity was measured using a Keithley 2400 SourceMeter under 4 point probe mode.

Electrochemical measurements

1 M $LiPF_6$ in ethylene carbonate (EC) and dimethyl carbonate (DMC) (v/v, 30/70) was used as electrolyte for the electrochemical measurements. The binder free electrode, the electrolyte, polypropylene separators, and Li metal foil were assembled into coin-type cells. Cyclic voltammetry tests were conducted at 0.1 mV/s in a voltage window of 4.0 – 2.0 V. Galvanostatic cycling measurements were conducted at 200 mA/g in a voltage window of 4.0 – 2.0 V. Rate capability tests were performed at current densities of 50, 200, 500 and 1000 mA/g. AC impedance data were collected in a frequency range of 100 kHz to 10 mHz with a voltage amplitude of 10 mV.

Vanadium K-edge (5.465 keV) X-ray absorption spectra (XAS) were collected at 10-BM-B at the Advanced Photon Source at Argonne National Laboratory. The XAS data were processed using the Athena and Artemis software packages,[53] where E_0 reference values (5.465 keV) from a V foil reference were used for calibration. The k range of 2-14 $Å^{-1}$ was used to obtain Fourier transformed extended X-ray absorption fine structure (EXAFS) spectra. k^2-weighted EXAFS spectra were displayed for analyses.

X-ray microfluorescence (µ-XRF) mapping with corresponding *operando* vanadium K-edge x-ray absorption near edge structure (XANES) measurements were collected at 5-ID of the National Synchrotron Light Source II (NSLS II) at Brookhaven National Laboratory. Cells with V_2O_5/CNT-3 cathode, lithium anode and 1 M $LiPF_6$ ethylene carbonate/dimethyl carbonate (3/7) electrolyte were discharged at 50 mA/g to $Li_{2.0}V_2O_5$. At 5-ID, the beam (0.5 µm × 0.5 µm) is focused via Kirkpatrick−Baez mirrors, energy is calibrated by Si(111) and Si(311) horizontal double-crystal monochromator, and a three-element VortexME3 silicon drift detector positioned at 90° to the incident beam is used for detection. µ-XRF mapping image of V_2O_5/CNT-3 was collected before discharge from a 190 µm x 200 µm sample area with step size of 5 µm. Energy was calibrated using a vanadium reference foil at 5.6 keV. Fluorescence mapping visualization and fitting was conducted using the Python-based beamline software.[54] The XANES spectra were aligned and normalized using Athena for VO_2 and V_2O_5 powder standards and V_2O_5/CNT-3 undischarged scan.[53] The pre-edge peaks were fit with a pseudo-Voigt function using Peakfit v4.12 software to determine absolute peak position as a function of lithiation from the raw data.

Scanning electron microscopy (SEM) and energy-dispersive X-ray spectroscopy (EDS) maps of the representative V_2O_5-CNT binder-free electrodes were probed using an analytical high-resolution SEM (JEOL 7600F) instrument, operating at an accelerating voltage of 10 kV. To

prepare samples for SEM characterization, V_2O_5-CNT binder-free electrodes samples were directly attached to a conductive carbon tape for subsequent image acquisition.

Energy dispersive X-ray diffraction (EDXRD) experiments were conducted at Argonne National Laboratories Advanced Photon Source (APS) beamline 6BM-B. A white beam was used to diffract X-rays from the active battery material inside the coin-type cells and was recorded using a germanium detector. In all experiments the detector angle from the measurement was $2\theta = 3^{o}$ and the gauge volume was 2 x 4 x 0.02 mm. The electrode was scanned from the Li anode to the stainless steel current collector in 0.02 mm increments. The acquisition time for each scan was 120 s. Cells were discharged at a rate of 50 mA/g in the voltage range of 2 – 4 V.

Electrode regeneration

After 100 cycles under a discharge and charge current of 200 mA/g, the binder free electrode was recovered from the cycled coin-type cell. Then the electrode was rinsed with DMC and dried. Thermal regeneration was performed by heating the recovered electrode at 300^{o}C for 2 h in air. The regenerated electrode was assembled into a new coin-type cell with fresh anode and electrolyte for galvanostatic cycling measurement.

Conflicts of Interest

There are no conflicts of interest to declare.

Acknowledgements

This work was supported as part of the Center for Mesoscale Transport Properties, an Energy Frontier Research Center supported by the U.S. Department of Energy, Office of Science, Basic Energy Sciences, under award DE-SC0012673. Experimental research characterizations were carried out in part at the Center for Functional Nanomaterials, Brookhaven National Laboratory, an Office of Science User Facility, which is supported by the U.S. Department of Energy, Office of Basic Energy Sciences, under Contract No. DE-SC0012704. The X-ray absorption spectroscopy measurements were performed at Beamline 10-BM-B of the Advanced Photon Source at Argonne National Laboratory, which are supported by the Department of Energy, under Contract No. DE-AC02-06CH11357. This research used Beamline 5-ID of the National Synchrotron Light Source II, a U.S. Department of Energy (DOE) Office of Science User Facility operated for the DOE Office of Science by Brookhaven National Laboratory under Contract No. DE-SC0012704. AMB acknowledges the support of the National Science Foundation Graduate Research Fellowship under grant No. 1109408. AA acknowledges support from the Graduate Assistance in Areas of National Need Fellowship. EST acknowledges the generous support of William and Jane Knapp including the Knapp Chair in Energy and the Environment.

References

1. D. Larcher and J. M. Tarascon, *Nature Chemistry*, 2014, **7**, 19.
2. J. Huang, L. M. Housel, C. D. Quilty, A. B. Brady, P. F. Smith, A. Abraham, M. R. Dunkin, D. M. Lutz, B. Zhang, E. S. Takeuchi, A. C. Marschilok and K. J. Takeuchi, *Journal of The Electrochemical Society*, 2018, **165**, A2849-A2858.
3. D. C. Bock, K. J. Takeuchi, A. C. Marschilok and E. S. Takeuchi, *Dalton Trans.*, 2013, **42**, 13981-13989.
4. X. Lin, J. Park, L. Liu, Y. Lee, A. M. Sastry and W. Lu, *Journal of The Electrochemical Society*, 2013, **160**, A1701-A1710.

5. C. J. Barnhart and S. M. Benson, *Energy & Environmental Science*, 2013, **6**, 1083-1092.
6. A. S. Poyraz, J. Huang, S. Cheng, D. C. Bock, L. Wu, Y. Zhu, A. C. Marschilok, K. J. Takeuchi and E. S. Takeuchi, *Green Chemistry*, 2016, **18**, 3414-3421.
7. X. Zhang, L. Li, E. Fan, Q. Xue, Y. Bian, F. Wu and R. Chen, *Chemical Society Reviews*, 2018, **47**, 7239-7302.
8. T. M. Gür, *Energy & Environmental Science*, 2018, **11**, 2696-2767.
9. J. Peters, D. Buchholz, S. Passerini and M. Weil, *Energy & Environmental Science*, 2016, **9**, 1744-1751.
10. B.-C. Yu, J.-W. Jung, K. Park and J. B. Goodenough, *Energy & Environmental Science*, 2017, **10**, 86-90.
11. Y. Shi, G. Chen and Z. Chen, *Green Chemistry*, 2018, **20**, 851-862.
12. J. B. Dunn, L. Gaines, J. C. Kelly, C. James and K. G. Gallagher, *Energy & Environmental Science*, 2015, **8**, 158-168.
13. M. Contestabile, S. Panero and B. Scrosati, *Journal of Power Sources*, 2001, **92**, 65-69.
14. J. Xu, H. Thomas, R. W. Francis, K. R. Lum, J. Wang and B. Liang, *Journal of Power Sources*, 2008, **177**, 512-527.
15. Q. Sa, E. Gratz, M. He, W. Lu, D. Apelian and Y. Wang, *J. Power Sources*, 2015, **282**, 140-145.
16. H. Zou, E. Gratz, D. Apelian and Y. Wang, *Green Chemistry*, 2013, **15**, 1183-1191.
17. K. Larsson and K. Binnemans, *Green Chem.*, 2014, **16**, 4595-4603.
18. L. Li, J. Lu, Y. Ren, X. X. Zhang, R. J. Chen, F. Wu and K. Amine, *Journal of Power Sources*, 2012, **218**, 21-27.
19. L. Yao, H. Yao, G. Xi and Y. Feng, *RSC Advances*, 2016, **6**, 17947-17954.
20. Q. Zhang, A. M. Bruck, D. C. Bock, J. Li, V. Sarbada, R. Hull, E. A. Stach, K. J. Takeuchi, E. S. Takeuchi and A. C. Marschilok, *Physical Chemistry Chemical Physics*, 2017.
21. L. Peng, Y. Zhu, D. Chen, R. S. Ruoff and G. Yu, *Advanced Energy Materials*, 2016, **6**, 1600025.
22. Y. Shi, G. Chen and Z. Chen, *Green Chem.*, 2018, **20**, 851-862.
23. H. Nie, L. Xu, D. Song, J. Song, X. Shi, X. Wang, L. Zhang and Z. Yuan, *Green Chemistry*, 2015, **17**, 1276-1280.
24. X. Meng, H. Cao, J. Hao, P. Ning, G. Xu and Z. Sun, *ACS Sustainable Chem. Eng.*, 2018, **6**, 5797-5805.
25. X. Meng, J. Hao, H. Cao, X. Lin, P. Ning, X. Zheng, J. Chang, X. Zhang, B. Wang and Z. Sun, *Waste Manage. (Oxford, U. K.)*, 2019, **84**, 54-63.
26. X. Wang, H. Qiu, H. Liu, P. Shi, J. Fan, Y. Min and Q. Xu, *Green Chem.*, 2018, **20**, 4901-4910.
27. Y.-K. Sun, S.-T. Myung, B.-C. Park, J. Prakash, I. Belharouak and K. Amine, *Nature Materials*, 2009, **8**, 320.
28. F. Lin, D. Nordlund, Y. Li, M. K. Quan, L. Cheng, T.-C. Weng, Y. Liu, H. L. Xin and M. M. Doeff, *Nature Energy*, 2016, **1**, 15004.
29. S.-K. Jung, H. Gwon, J. Hong, K.-Y. Park, D.-H. Seo, H. Kim, J. Hyun, W. Yang and K. Kang, *Advanced Energy Materials*, 2014, **4**, 1300787-n/a.
30. Y. Xie, M. Saubanère and M.-L. Doublet, *Energy & Environmental Science*, 2017, **10**, 266-274.
31. C. Delmas, H. Cognac-Auradou, J. Cocciantelli, M. Menetrier and J. Doumerc, *Solid State Ionics*, 1994, **69**, 257-264.
32. A. Q. Pan, H. B. Wu, L. Zhang and X. W. D. Lou, *Energy & Environmental Science*, 2013, **6**, 1476-1479.
33. S. Wang, Z. Lu, D. Wang, C. Li, C. Chen and Y. Yin, *Journal of Materials Chemistry*, 2011, **21**, 6365-6369.

34. Y. Li, J. Yao, E. Uchaker, J. Yang, Y. Huang, M. Zhang and G. Cao, *Advanced Energy Materials*, 2013, **3**, 1171-1175.
35. J. Lee, S. Badie, P. Srimuk, A. Ridder, H. Shim, S. Choudhury, Y.-C. Nah and V. Presser, *Sustainable Energy & Fuels*, 2018, **2**, 577-588.
36. J. Cocciantelli, M. Menetrier, C. Delmas, J. Doumerc, M. Pouchard, M. Broussely and J. Labat, *Solid State Ionics*, 1995, **78**, 143-150.
37. Z. Chen, V. Augustyn, J. Wen, Y. Zhang, M. Shen, B. Dunn and Y. Lu, *Advanced Materials*, 2011, **23**, 791-795.
38. J. Wu, X. Gao, H. Yu, T. Ding, Y. Yan, B. Yao, X. Yao, D. Chen, M. Liu and L. Huang, *Advanced Functional Materials*, 2016, **26**, 6114-6120.
39. M. M. Doroodmand, S. Sobhani and A. Ashoori, *Canadian Journal of Chemistry*, 2012, **90**, 701-707.
40. Y. Liu, G. Gao, X. Liang and G. Wu, *Journal of Solid State Electrochemistry*, 2018, **22**, 2385-2393.
41. Y. Zhang, Y. Wang, Z. Xiong, Y. Hu, W. Song, Q.-a. Huang, X. Cheng, L.-Q. Chen, C. Sun and H. Gu, *ACS Omega*, 2017, **2**, 793-799.
42. H. Song, C. Liu, C. Zhang and G. Cao, *Nano Energy*, 2016, **22**, 1-10.
43. T. Zhai, H. Liu, H. Li, X. Fang, M. Liao, L. Li, H. Zhou, Y. Koide, Y. Bando and D. Golberg, *Advanced Materials*, 2010, **22**, 2547-2552.
44. C. Delmas, S. Brethes and M. Menetrier, *Journal of power sources*, 1991, **34**, 113-118.
45. J. Wong, F. W. Lytle, R. P. Messmer and D. H. Maylotte, *Physical Review B*, 1984, **30**, 5596-5610.
46. G. A. Horrocks, E. J. Braham, Y. Liang, L. R. De Jesus, J. Jude, J. M. Velázquez, D. Prendergast and S. Banerjee, *The Journal of Physical Chemistry C*, 2016, **120**, 23922-23932.
47. C. Delmas, H. Cognac-Auradou, J. M. Cocciantelli, M. Ménétrier and J. P. Doumerc, *Solid State Ionics*, 1994, **69**, 257-264.
48. J. Kawakita, T. Kato, Y. Katayama, T. Miura and T. Kishi, *Journal of Power Sources*, 1999, **81-82**, 448-453.
49. P. Scherrer, *Nachr. Ges. Wiss. Göttingen*, 1918, **2**, 96-100.
50. F. Benzi, G. Giuli, S. Della Longa and E. Paris, *Journal of synchrotron radiation*, 2016, **23**, 947-952.
51. B. Joseph, A. Iadecola, L. Maugeri, M. Bendele, M. Okubo, H. Li, H. Zhou, T. Mizokawa and N. Saini, *Applied Physics Letters*, 2013, **103**, 251910.
52. G. Berckmans, M. Messagie, J. Smekens, N. Omar, L. Vanhaverbeke and J. Van Mierlo, *Energies*, 2017, **10**.
53. B. Ravel and M. Newville, *Physica Scripta*, 2005, **2005**, 1007.
54. L. Li, H. Yan, W. Xu, D. Yu, A. Heroux, W.-K. Lee, S. I. Campbell and Y. S. Chu, in *SPIE Optical Engineering + Applications*, SPIE, 2017, p. 8.

Figures

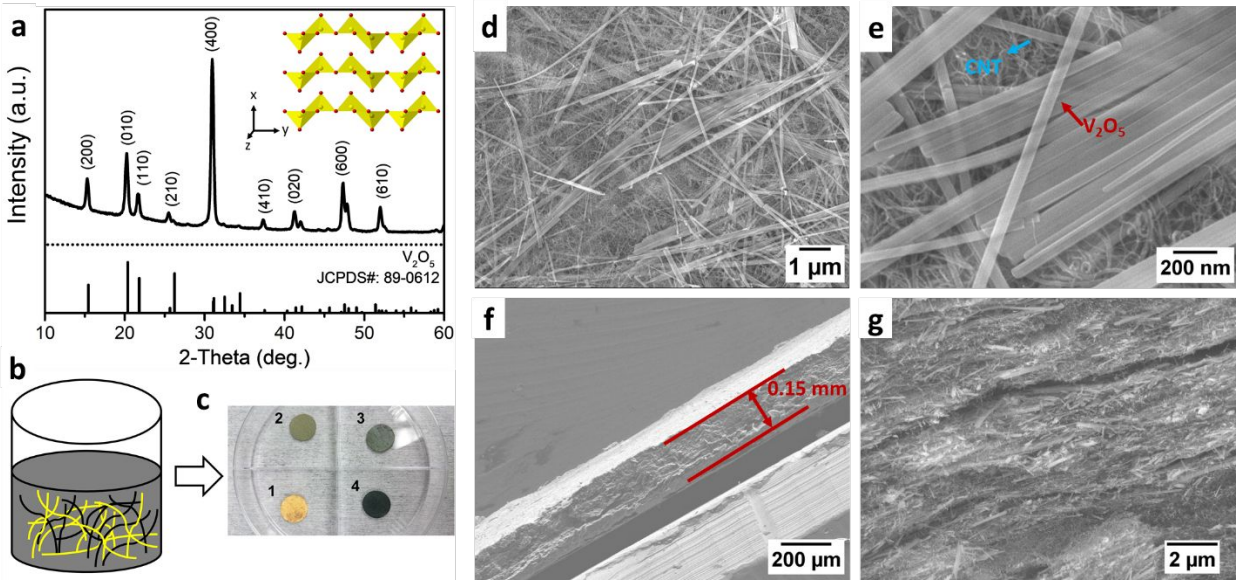

Figure 1. (a) XRD pattern of as-synthesized V_2O_5. (b) Schematic of the preparation of V_2O_5/CNT electrodes. (c) Digital images of V_2O_5/CNT electrodes. (d, e) Representative top-view and (f, g) side-view SEM images of the V_2O_5/CNT-3 binder-free electrodes under different magnifications.

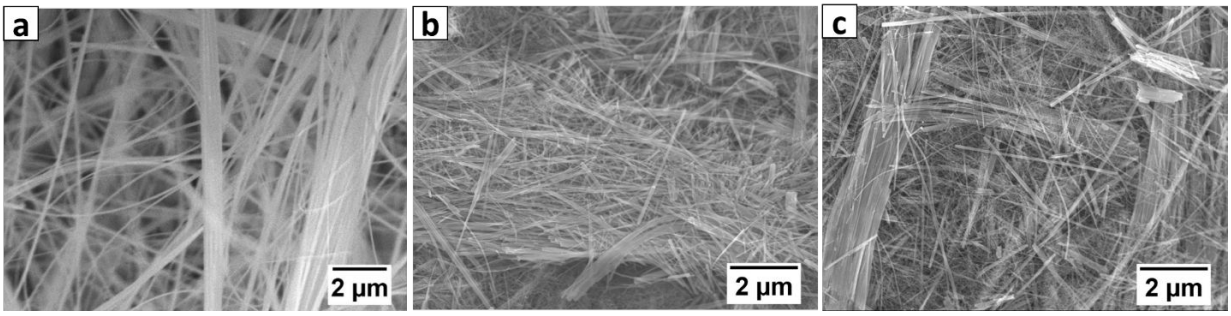

Figure 2. Representative top-view images of (a) V_2O_5/CNT-0, (b) V_2O_5/CNT-1, and (c) V_2O_5/CNT-2 binder-free electrodes.

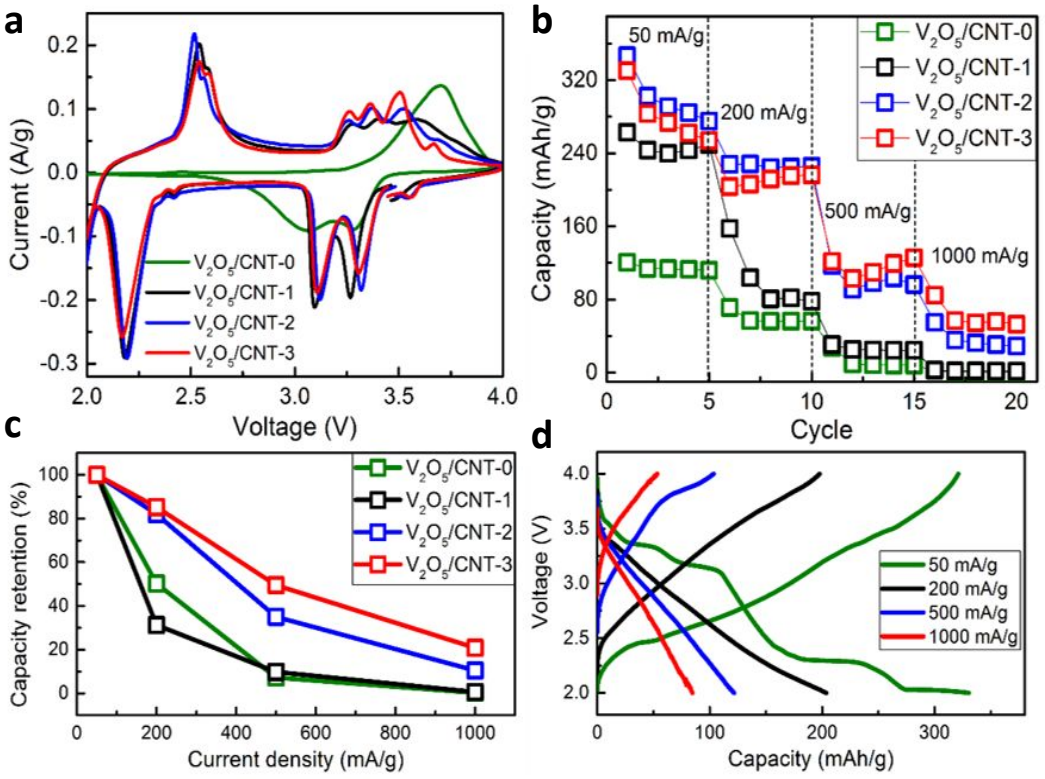

Figure 3. (a) Cyclic voltammetry, (b) rate capability, and (c) capacity retention at different current densities of the V_2O_5/CNT electrodes in lithium based electrochemical cells. (d) Discharge-charge curves of V_2O_5/CNT-3 at different current densities.

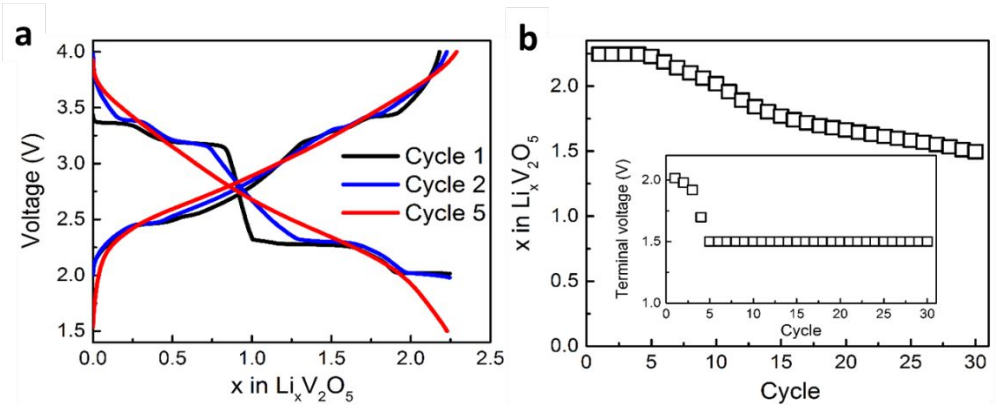

Figure 4. V_2O_5/CNT-3 tested under repetitive 2.25 electron equivalent Coulombically controlled reduction with a secondary voltage limit of 1.5 V (a) Discharge-charge curves for Cycles 1, 2, and 5. (b) Lithiation level as a function of cycle number. Inset: terminal discharge voltages as a function of cycle number.

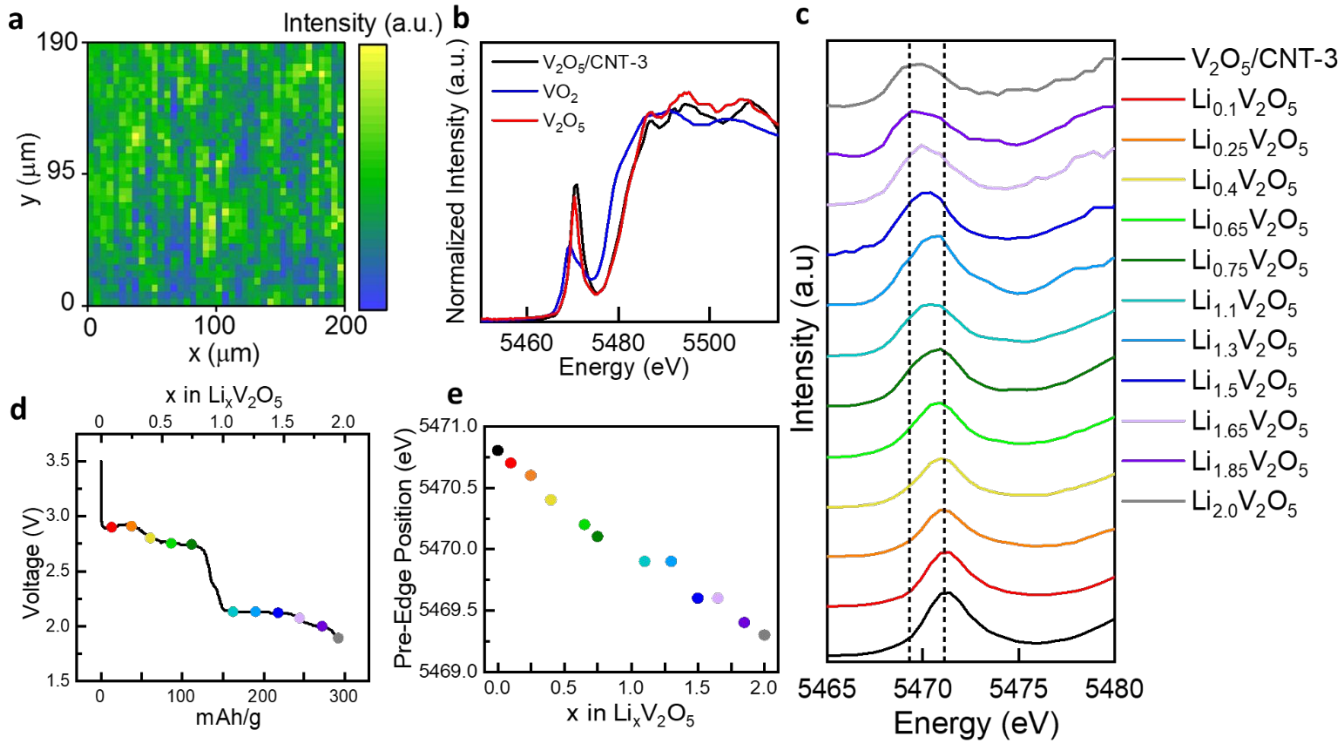

Figure 5. (a) μ-XRF map of pristine V_2O_5/CNT-3 electrode. (b) XANES comparison of pristine V_2O_5/CNT-3 electrode and V_2O_5 and VO_2 powder standards. (c) XANES pre-edge region as function of lithiation for V_2O_5/CNT-3. (d) Discharge curve for operando-V_2O_5/CNT-3 cell at 50 mA/g to $Li_{2.0}V_2O_5$. Markers indicate the beginning of the XANES measurements. (e) Pre-edge peak positions as function of state of lithiation.

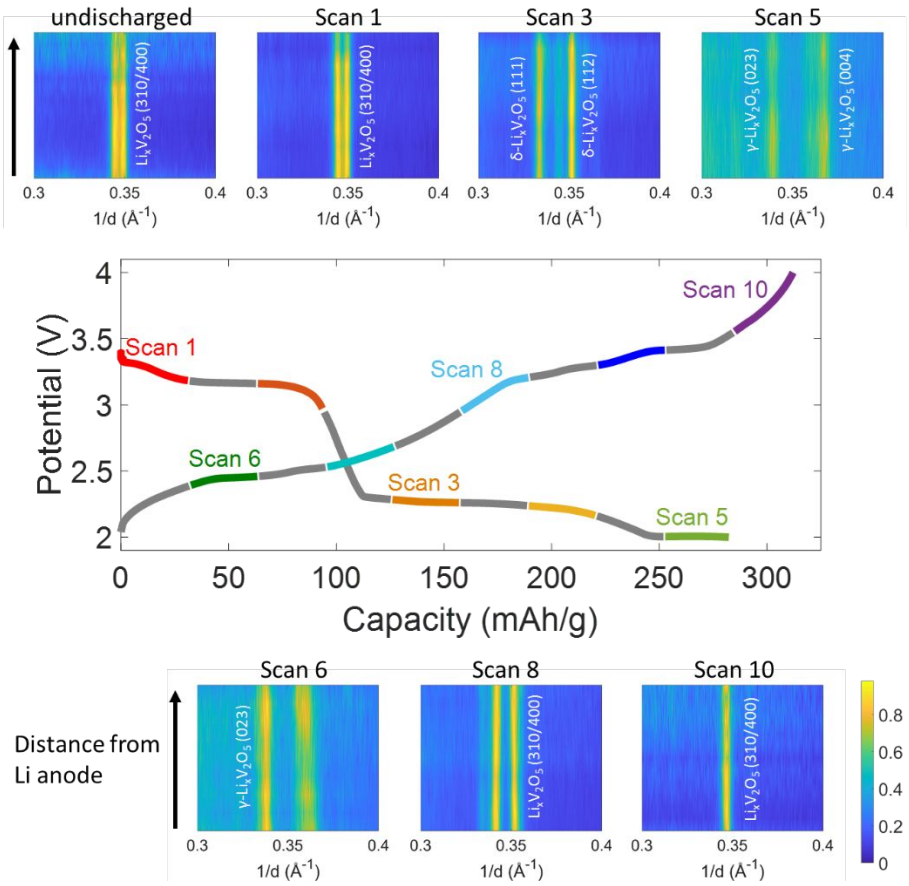

Figure 6. EDXRD scans and voltage profile of the first lithiation-delithiation cycle of the V_2O_5-CNT electrode at a rate of 50 mA/g. Capacities when the scans were collected are identified on the discharge and charge curves. Each set of scans is shown between 0.3-0.4 Å^{-1} to show evolution of the V_2O_5 (400) peak.

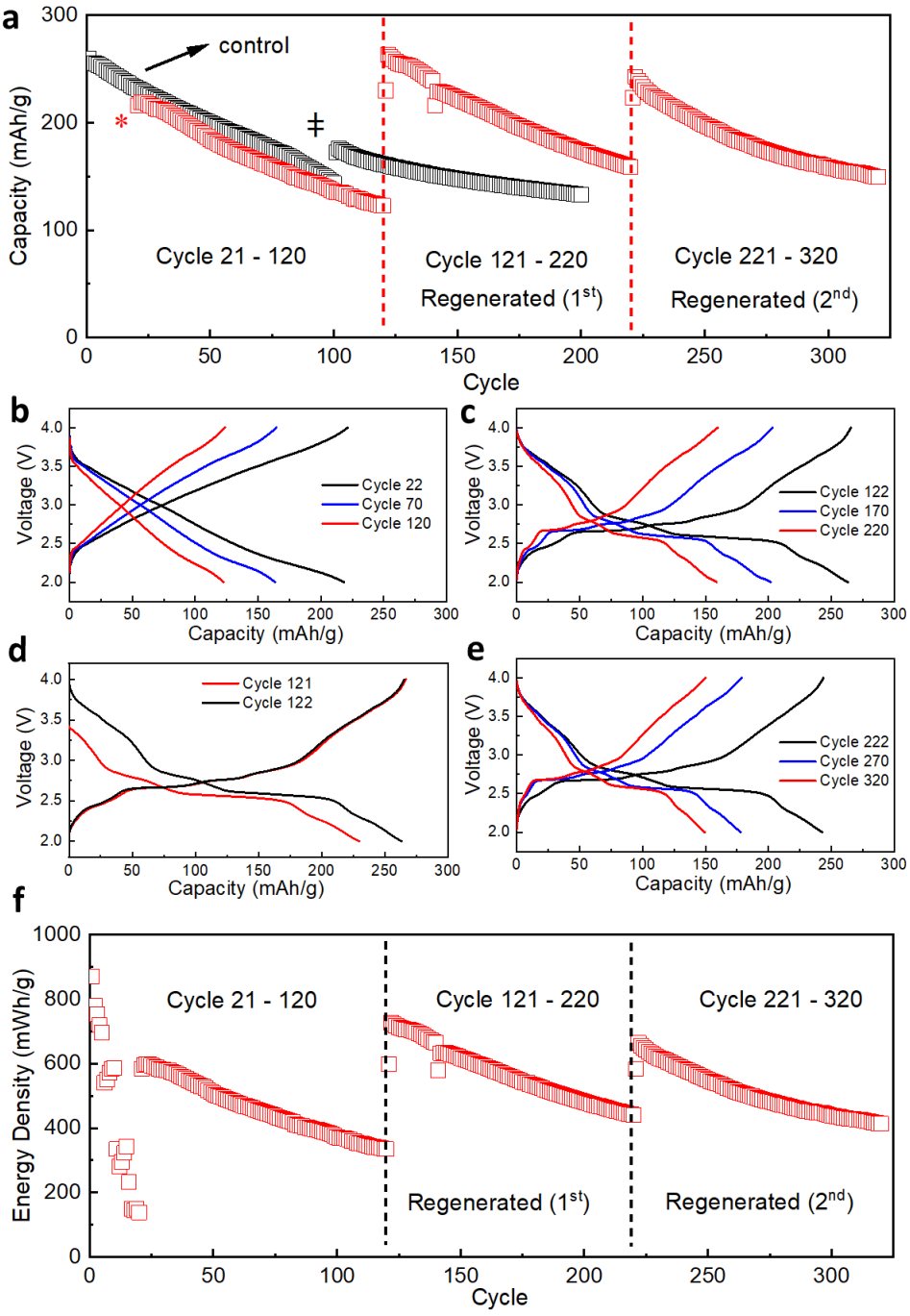

Figure 7. (a) Lithiation and delithiation of V_2O_5/CNT-3 under a current density of 200 mA/g. The test electrode (red) was cycled for 100 cycles, recovered and then thermally regenerated and reassembled in a fresh cell. This process was repeated two times. *Cycles 1-20 involved a rate capability test represented in Figure 3b. The control electrode (black) was cycled for 100 cycles, recovered and reassembled in a fresh cell without thermal regeneration. ǂ Discontinuity at Cycle 100 is attributed to recovery. Discharge-charge curves of V_2O_5/CNT-3 (b) before regeneration, and (c) after the 1st regeneration. (d) First two discharge-charge curves of the 1st regenerated V_2O_5/CNT-3 electrode. (e) Discharge-charge curves of the 2nd regenerated V_2O_5/CNT-3

electrode at Cycles 222, cycle 270, and cycle 320. (f) Energy densities of regeneration test electrode under rate capability test (cycles 1-20) and extended cycling at 200 mA/g (cycles 121-320).

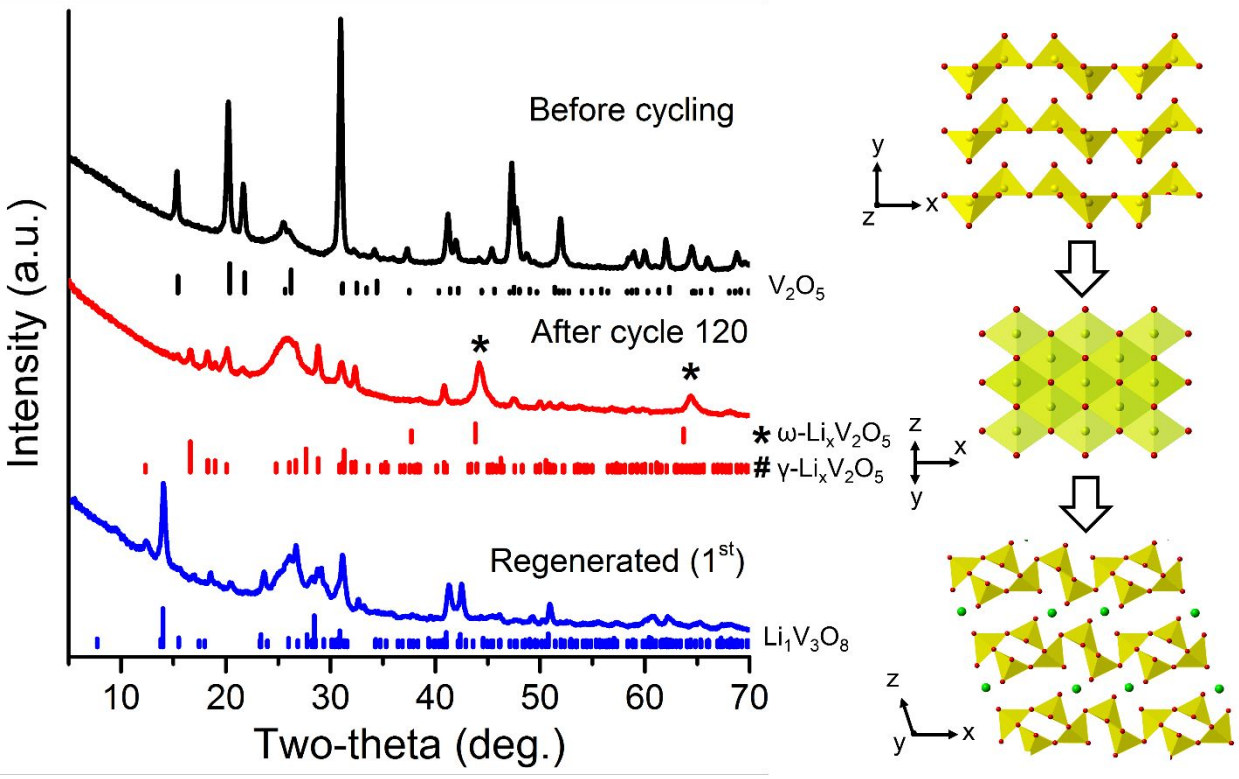

Figure 8. XRD patterns of V_2O_5/CNT-3 electrode (top) before cycling, (middle) after 120 cycles, and (bottom) after the 1st regeneration. Inset: crystal structures of (top) V_2O_5, (middle) ω-LiV_2O_5, and (bottom) $Li_1V_3O_8$.

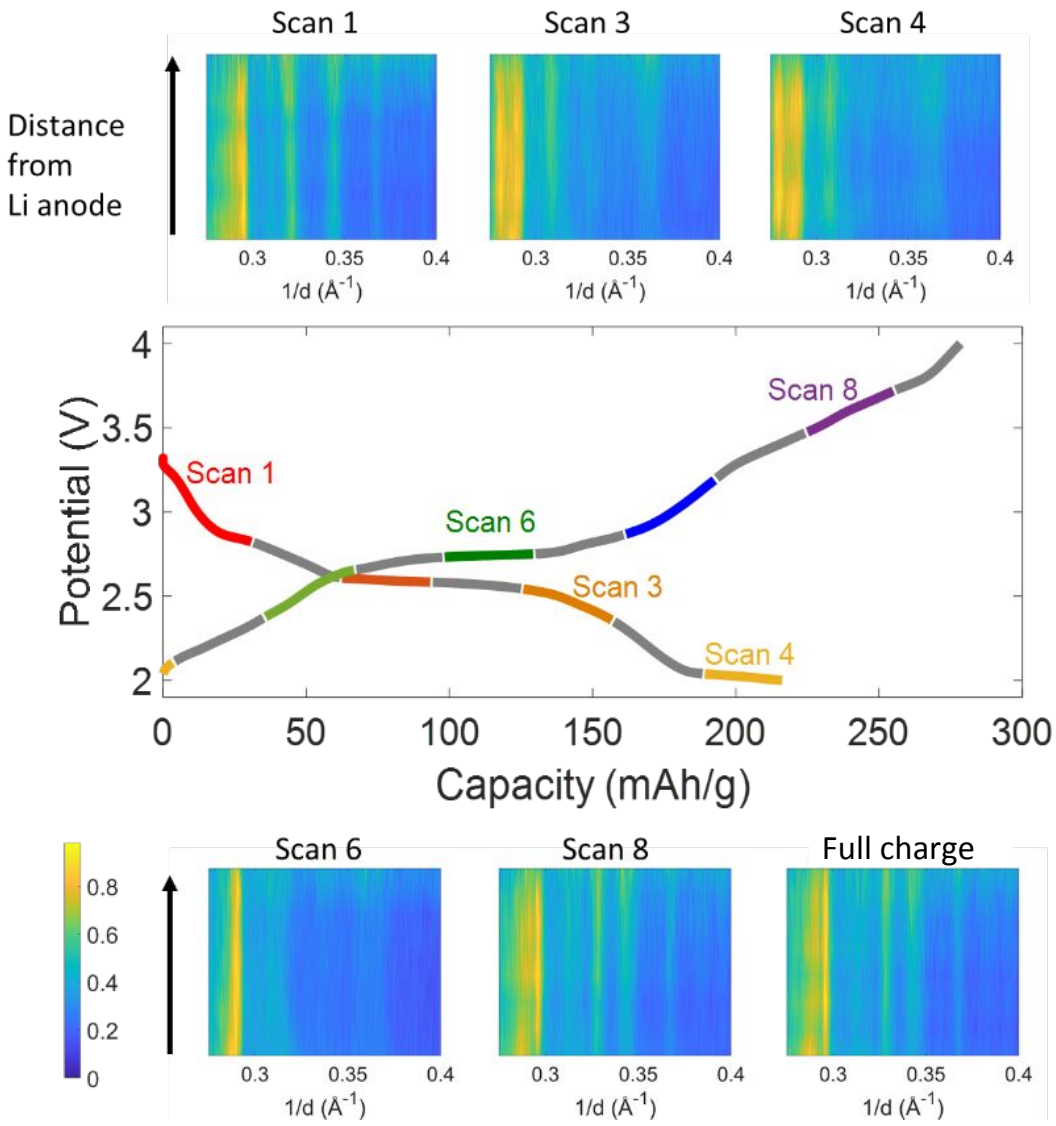

Figure 9. EDXRD scans and voltage profile of the first cycle of the regenerated V_2O_5/CNT electrode at a rate of 50 mA/g. Scans are identified on the (dis)charge curve and each scan is shown from 0.27-0.4 Å^{-1}.

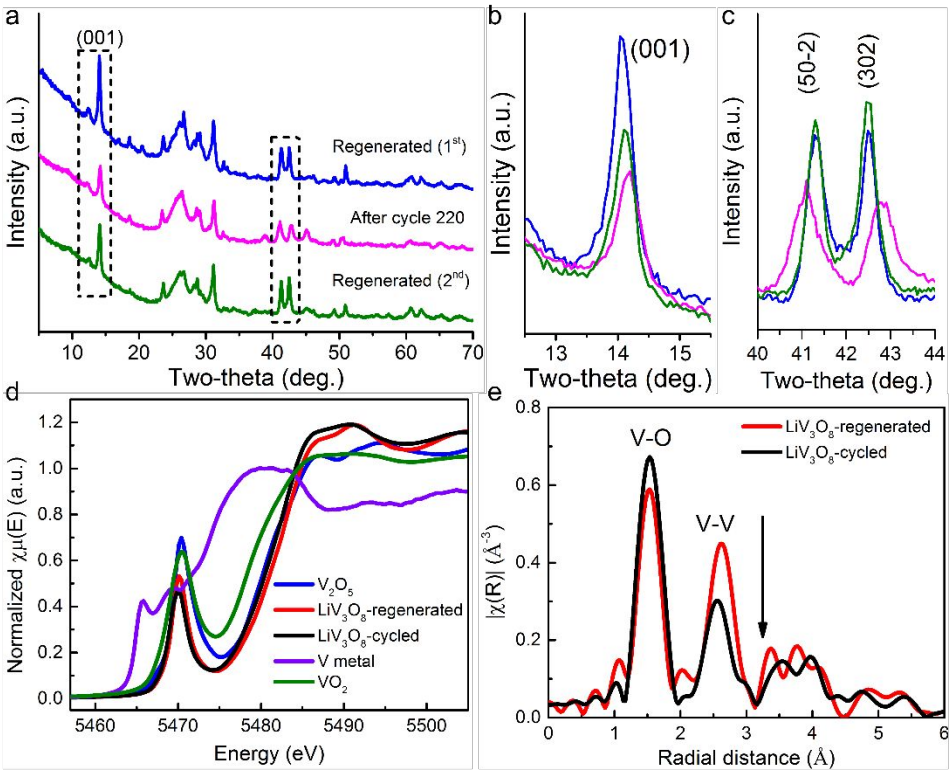

Figure 10. (a) XRD patterns of V_2O_5/CNT-3 electrode after the 1st regeneration, cycle 220, and the 2nd regeneration. (b) and (c) Comparisons of XRD diffraction peaks. (d) XANES and (e) EXAFS spectra of the regenerated and cycled electrode.

Table 1. Calculated crystallite sizes after the 1st regeneration, cycle 220, and the 2nd regeneration.

Diffraction plane	Sample	2-theta (°)	FWHM	Crystallite size (nm)
(001)	Regenerated (1st)	14.1	0.345	39
	After cycle 220	14.2	0.437	27
	Regenerated (2nd)	14.1	0.349	38
(50-2)	Regenerated (1st)	41.3	0.470	26
	After cycle 220	41.1	0.632	18
	Regenerated (2nd)	41.3	0.443	28
(302)	Regenerated (1st)	42.5	0.396	33
	After cycle 220	42.8	0.605	19
	Regenerated (2nd)	42.5	0.417	31